Inorganic Chemistry

ARTICLE

pubs.acs.org/IC

# Electronic Optimization of Heteroleptic Ru(II) Bipyridine Complexes by Remote Substituents: Synthesis, Characterization, and Application to Dye-Sensitized Solar Cells

Won-Sik Han,[†] Jung-Kyu Han,[†] Hyun-Young Kim,[†] Mi Jin Choi,[‡] Yong-Soo Kang,[‡] Chyongjin Pac,*[,†] and Sang Ook Kang*[,†]

[†]Department of Advanced Material Chemistry, Korea University, Sejong, Chungnam 339-700, South Korea

[‡]WCU Department of Energy Engineering and Center for Next Generation Dye-sensitized Solar Cells, Hanyang University, Seoul 133-791, South Korea

Supporting Information

**ABSTRACT:** We prepared a series of new heteroleptic ruthenium(II) complexes, $Ru(NCS)_2LL'$ (**3a**−**3e**), where L is 4,4′-di(hydroxycarbonyl)-2,2′-bipyridine and L′ is 4,4′-di(*p*-X-phenyl)-2,2′-pyridine (X = CN (**a**), F (**b**), H (**c**), OMe (**d**), and $NMe_2$ (**e**)), in an attempt to explore the structure−activity relationships in their photophysical and electrochemical behavior and in their performance in dye-sensitized solar cells (DSSCs). When substituent X is changed from electron-donating $NMe_2$ to electron-withdrawing CN, the absorption and emission maxima reveal systematic bathochromic shifts. The redox potentials of these dyes are also significantly influenced by X. The electronic properties of the dyes were theoretically analyzed using density functional theory calculations; the results show good correlations with the experimental results. The solar-cell performance of DSSCs based on dye-grafted nanocrystalline $TiO_2$ using **3a**−**3e** and standard **N3** (bis[(4,4′-carboxy-2,2′-bipyridine)(thiocyanato)]ruthenium(II)) were compared, revealing substantial dependences on the dye structures, particularly on the remote substituent X. The **3d**-based device showed the best performance: $\eta$ = 8.30%, $J_{SC}$ = 16.0 mA·cm$^{-2}$, $V_{OC}$ = 717 mV, and ff = 0.72. These values are better than **N3**-based device.

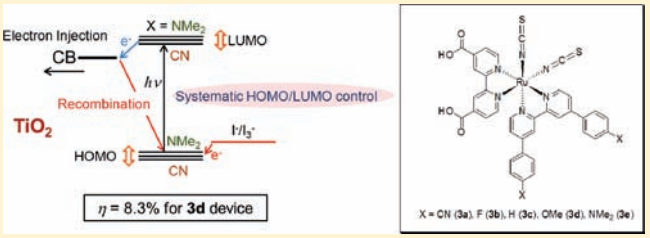


## INTRODUCTION

The development of systems for converting solar energy into chemical fuels or electricity is among the most demanding challenges that chemists face today. In light harvesting, the first step in such conversion, the choice of a photosensitizer capable of efficient visible-light absorption is crucial. Therefore, many efforts have focused on the design and synthesis of various dyes, including metal complexes[1−3] and organic dyes.[4,5] Among them, Ru(II) polypyridine complexes[1] have been intensively pursued as a potential candidate for efficient sensitizers because of their favorable photophysical properties, such as intense charge-transfer (CT) absorption in the visible range and moderately intense emission with fairly long lifetimes in fluid solutions at ambient temperature. They also exhibit reversible redox behavior with tunable potentials.[6] Consequently, a variety of Ru(II) complexes have been extensively applied to photoinduced hydrogen evolution,[7] $CO_2$ reduction,[8] and dye-sensitized solar cells (DSSCs).[9] For the development of DSSCs, $Ru(NCS)_2L_2$ (L = 4,4′-di(hydroxycarbonyl)-2,2′-bipyridine, called **N3** dye) is regarded as a key molecule; it displays intense visible-light absorption and rapid electron injection from the excited states into the conduction band of $TiO_2$.[1e,9e] Thus, one of the basic strategies underlying the molecular design of efficient sensitizers has been the modification of **N3** dye based on heteroleptic complexes $Ru(NCS)_2LL'$. The aim is mainly to (1) broaden the absorption range and increase the molar absorption coefficients by extending the conjugation length of L′[10] and (2) tune the highest occupied molecular orbital/lowest unoccupied molecular orbital (HOMO/LUMO) levels by introducing other $\sigma$-donor ligands and L′.[11] Attempts have been made using polypyridine ligands (L′) conjugated with a $\pi$ system such as thiophene,[12] thienothiophene,[13] alkoxybenzene moieties,[14] or ethenyl-linked phenyl groups.[15] Alternative approaches are based on the tuning of the light absorption to lower energies by introducing a ligand with a low-lying $\pi^*$ molecular orbital[16] and/or by destabilization of the metal $t_{2g}$ orbital with a strong donor ligand.[17]

In this work, we focused on the structure−property relationships of $Ru(NCS)_2LL'$ by using 4,4′-di(*p*-X-phenyl)-2,2′-bipyridine as L′. Significant $\pi$-conjugation of the phenyl rings should certainly enlarge both the absorption range and the CT cross section of relevant Ru(II) complexes. Furthermore, the remote substituent (X) might provide indirect electronic perturbations to relevant Ru(II) complexes through the phenyl rings, with a

**Received:** September 17, 2010
**Published:** March 21, 2011

potential for fine-tuning the HOMO/LUMO levels. Therefore, we have prepared **N3**-dye-related heteroleptic complexes, Ru(NCS)$_2$LL′ (L′ = 4,4′-di(*p*-X-phenyl)-2,2′-pyridine), in which substituent X is strong electron-withdrawing CN (**3a**), weakly electron-withdrawing F (**3b**) and H (**3c**), moderately electron-donating OMe (**3d**), or strong electron-donating NMe$_2$ (**3e**). With this series of Ru(II) complexes, we have found that by varying X, we can fine-tune the lowest metal-to-ligand charge transfer (MLCT) band position and the electrochemical redox potentials associated with the HOMO/LUMO levels of the ruthenium polypyridyl complexes. In this study, we report the preparation of Ru(NCS)$_2$LL′ complexes, their photophysical and electrochemical behavior, and their possible application to DSSCs. A DSSC using Ru(NCS)$_2$LL′ with X = OMe (**3d**) shows the best performance among the devices, with a higher power conversion efficiency than **N3** dye under identical conditions of cell fabrication and measurement.

## EXPERIMENTAL SECTION

**General Procedures.** Unless stated otherwise, all reagents were purchased from Aldrich and used without further purification. Dry acetonitrile was distilled over calcium hydride powder under argon. Toluene was distilled over sodium and benzophenone ketyl before use. *N*,*N*-dimethylformamide (DMF) was distilled from calcium hydride and stored over 4 Å molecular sieves. 4,4′-Dinitro-2,2′-bipyridine *N*,*N*′-dioxide was synthesized according to the literature.[18] NMR spectra were recorded on a Varian Mercury 300 spectrometer operating at 300.1 MHz for $^1$H and 75.4 MHz for $^{13}$C. The chemical shift of the chloroform or DMSO-$d_6$ signal was used as a reference ($\delta$ = 7.26 or 2.49 ppm for $^1$H and $\delta$ = 77.0 or 39.5 ppm for $^{13}$C, respectively). Elemental analyses (Carlo Erba Instruments CHNS-O EA 1108 analyzer) and high-resolution tandem mass spectrometry (Jeol LTD JMS-HX 110/110A) were performed at the Ochang Branches of the Korean Basic Science Institute. Absorption and photoluminescence spectra were recorded on a Shimadzu UV-3101PC UV−vis-NIR scanning spectrophotometer and a Varian Cary Eclipse fluorescence spectrophotometer, respectively. Cyclic voltammetry experiments were conducted on a BAS 100 electrochemical analyzer equipped with a three-electrode cell system (a glassy carbon working electrode, a platinum wire counter-electrode, and a Ag/AgNO$_3$ reference electrode). Freshly distilled, degassed acetonitrile was used as the solvent, and 0.1 M tetrabutylammonium tetrafluoroborate was used as the supporting electrolyte. Potentials were initially referenced to an internal ferrocene (Fc) standard.

**Synthesis of 4,4′-Dibromo-2,2′-bipyridine *N*,*N*′-dioxide.** A suspension of 4,4′-dinitro-2,2′-bipyridine *N*,*N*′-dioxide[18] (13.6 mmol, 3.8 g) in glacial acetic acid (60 mL) and acetyl bromide (40 mL) was stirred for 4 h at 100 °C. The resulting yellow-brown solution was cooled to 0 °C, poured onto ice (125 g), and then neutralized with a concentrated sodium hydroxide solution. An off-white solid was filtered off, washed with water, and air-dried to give 4,4′-dibromo-2,2′-bipyridine *N*,*N*′-dioxide in 80% yield (2.8 g). $^1$H NMR (300.1 MHz; DMSO-$d_6$ + $CF_3COOH$); $\delta$ 8.29 (d, 2H), 8.03 (d, 2H), 7.78 (dd, 2H); Anal. Calcd for $C_{10}H_6Br_2N_2O_2$ (345.97): C, 34.72; H, 1.75; N, 8.10; Found: C, 34.32; H, 1.92; N, 8.20.

**Synthesis of 4,4′-Dibromo-2,2′-bipyridine.** A suspension of 4,4′-dibromo-2,2′-bipyridine *N*,*N*′-dioxide (2.2 mmol, 0.58 g) and $PBr_3$ (46 mmol, 12.5 g) in anhydrous acetonitrile (100 mL) was refluxed for 4 h. The resulting yellow-brown solution was poured into ice water (200 g). After the solution was adjusted to pH 11 with concentrated sodium hydroxide solution, a yellow-white suspension formed and was extracted exhaustively with $CHCl_3$. The combined organic layers were dried over $Na_2CO_3$ and then evaporated under reduced pressure. Recrystallization from water/ethanol produced small off-white crystals in 90% yield (0.45 g). mp 130 °C; $^1$H NMR (300.1 MHz; $CDCl_3$); $\delta$ 8.61 (d, 2H), 8.48 (2H, d), 7.50 (2H, dd); HRMS (FAB) calcd for $C_{10}H_6Br_2N_2$: 311.8898. Found: 311.8911 $[M]^+$; Anal. Calcd for $C_{10}H_6Br_2N_2$: C, 38.25; H, 1.93; Found: C, 38.23; H, 1.94.

**General Procedure for Suzuki Coupling of 4,4′-Dibromo-2,2′-bipyridine.** An oven-dried Schlenk flask was evacuated and backfilled with nitrogen. The reaction flask was charged with corresponding boronic acid (10 mmol), 4,4′-dibromo-2,2′-bipyridine (4 mmol, 1.26 g), toluene (80 mL), and aqueous sodium carbonate solution (2 M, 35 mL). After the biphasic mixture was bubbled for 15 min by nitrogen stream, $Pd(PPh_3)_4$ (5 mol % based on 4,4′-dibromo-2,2′-bipyridine, 0.23 g) was added, and the mixture was refluxed for 14 h. After the mixture cooled to room temperature, the aqueous layer was separated and extracted with $CH_2Cl_2$ (3 × 50 mL). The combined organic layers were washed with brine, dried over anhydrous magnesium sulfate, filtered, and concentrated in vacuo. The crude material was purified by flash chromatography on silica gel.

**4,4′-Bis(*p*-cyanophenyl)-2,2′-bipyridine (2a).** The coupling of 4,4′-dibromo-2,2′-bipyridine (4 mmol, 1.26 g) with 4-cyanophenylboronic acid (10 mmol, 1.47 g) was effected using the general procedure with 5 mol % $Pd(PPh_3)_4$ (0.23 g). Flash chromatography using a 15:1 dichloromethane/methanol eluent gave the title compound as an off-white powder in 78% yield (1.12 g). $^1$H NMR (300.1 MHz; $CDCl_3$); $\delta$ 8.78 (t, 2H), 8.73 (s, 2H), 7.86 (dd, 4H), 7.80 (dd, 4H), 7.55 (dd, 2H); HRMS (FAB) calcd for $C_{24}H_{14}N_4$: 358.1218. Found: 359.1221 $[M + H]^+$; Anal. Calcd for $C_{24}H_{14}N_4$: C, 80.43; H, 3.94; N, 15.63; Found: C, 80.35; H, 3.92; N, 15.66.

**4,4′-Bis(*p*-fluorophenyl)-2,2′-bipyridine (2b).** The coupling of 4,4′-dibromo-2,2′-bipyridine (4 mmol, 1.26 g) with 4-fluorophenylboronic acid (10 mmol, 1.40 g) was effected using the general procedure with 5 mol % $Pd(PPh_3)_4$ (0.23 g). Flash chromatography using a 15:1 dichloromethane/methanol eluent gave the title compound as an off-white powder in 88% yield (1.21 g). $^1$H NMR (300.1 MHz; $CDCl_3$); $\delta$ 8.71 (d, 2H), 8.65 (s, 2H), 7.73 (dd, 4H), 7.49 (dd, 2H), 7.17 (dd, 4H); $^{13}$C NMR $\delta$ 164.5, 156.7, 149.9, 148.6, 134.5, 129.2, 122.3, 119.3, 116.4; HRMS (FAB) calcd for $C_{22}H_{14}F_2N_2$: 344.1125. Found: 345.1132 $[M + H]^+$; Anal. Calcd for $C_{22}H_{14}F_2N_2$: C, 76.73; H, 4.10; N, 8.13; Found: C, 76.71; H, 4.09; N, 8.14.

**4,4′-Diphenyl-2,2′-bipyridine (2c).** The coupling of 4,4′-dibromo-2,2′-bipyridine (4 mmol, 1.26 g) with phenylboronic acid (10 mmol, 1.21 g) was effected using the general procedure with 5 mol % Pd$(PPh_3)_4$ (0.23 g). Flash chromatography using a 10:1 dichloromethane/methanol eluent gave the title compound as an off-white powder in 93% yield (1.15 g). $^1$H NMR (300.1 MHz; $CDCl_3$); $\delta$ 8.73 (d, 2H), 8.71 (s, 2H), 7.77 (dd, 4H), 7.54 (dd, 2H), 7.49 (dd, 4H), 7.43 (dd, 2H); $^{13}$C NMR $\delta$ 156.9, 149.9, 149.6, 138.5, 129.3, 127.4, 121.9, 119.5; HRMS (FAB) calcd for $C_{22}H_{16}N_2$: 308.1313. Found: 308.1319 $[M]^+$; Anal. Calcd for $C_{22}H_{16}N_2$: C, 85.69; H, 5.23; N, 9.08; Found: C, 85.67; H, 5.21; N, 9.09.

**4,4′-Bis(*p*-methoxyphenyl)-2,2′-bipyridine (2d).** The coupling of 4,4′-dibromo-2,2′-bipyridine (4 mmol, 1.26 g) with 3-methoxyphenylboronic acid (10 mmol, 1.52 g) was effected using the general procedure with 5 mol % $Pd(PPh_3)_4$ (0.23 g). Flash chromatography using a 15:1 dichloromethane/methanol eluent gave the title compound as an off-white powder in 91% yield (1.34 g). $^1$H NMR (300.1 MHz; $CDCl_3$); $\delta$ 8.69 (d, 2H), 8.65 (s, 2H), 7.73 (dd, 4H), 7.50 (dd, 2H), 7.00 (dd, 4H), 3.85 (s, 6H); $^{13}$C NMR $\delta$ 160.7, 156.8, 149.8, 149.0, 130.7, 128.6, 121.3, 118.8, 114.6, 55.6; HRMS (FAB) calcd for $C_{24}H_{20}N_2O_2$: 368.1525. Found: 368.1531 $[M]^+$; Anal. Calcd for $C_{24}H_{20}N_2O_2$: C, 78.24; H, 5.47; N, 7.60; Found: C, 78.20; H, 5.45; N, 7.62.

**4,4′-Bis(*p*-dimethylaminophenyl)-2,2′-bipyridine (2e).** The coupling of 4,4′-dibromo-2,2′-bipyridine (4 mmol, 1.26 g) with 4-(dimethylamino)phenylboronic acid (10 mmol, 1.65 g) was effected

using the general procedure with 5 mol % $Pd(PPh_3)_4$ (0.23 g). Flash chromatography using a 15:1 dichloromethane/methanol eluent gave the title compound as an off-white powder in 37% yield (0.58 g). $^1$H NMR (300.1 MHz; $CDCl_3$); $\delta$ 8.62 (s, 2H), 8.51 (d, 2H), 7.71 (dd, 4H), 7.52 (dd, 2H), 7.48 (dd, 2H), 6.80 (d, 4H), 3.03 (s, 12H); HRMS (FAB) calcd for $C_{26}H_{26}N_4$: 394.2157. Found: 395.2168 $[M + H]^+$; Anal. Calcd for $C_{26}H_{26}N_4$: C, 79.16; H, 6.64; N, 14.20; Found: C, 79.13; H, 6.68; N, 14.22.

**General Procedure for Conventional One-Pot Synthesis of $Ru(NCS)_2LL'$.** To a solution of dichloro(*p*-cymene)ruthenium(II) dimer (0.11 g, 0.17 mmol) and L′ (**2a**−**2e**) (0.34 mmol) in DMF (50 mL) heated at 80 °C for 4 h under $N_2$ in the dark, and then 2,2′-bipyridine-4,4′-dicarboxylic acid (L) (0.08 g, 0.34 mmol) was added. The reaction mixture was stirred at 140 °C for 4 h. After an excess of $NH_4NCS$ (1.05 g, 13.7 mmol) was added to the resulting dark solution, the mixture was stirred for another 4 h at 140 °C and then cooled to room temperature. After the removal of DMF under vacuum followed by the addition of water, the suspended solution was filtered on a sintered glass crucible by suction filtration to give a solid. After washing with water and with diethyl ether, the crude complex was dissolved in basic methanol (tetrabutylammonium hydroxide) and purified on a Sephadex LH-20 column using methanol as the eluent. The collected main band was concentrated and slowly titrated with an acidic methanol solution ($HNO_3$) to pH 3.1. It should be noted that this titration should be done very slowly. The precipitate was collected on a sintered glass crucible by suction filtration and dried under air.

**3a** (X = CN): yield 72%; $^1$H NMR (300.1 MHz; DMSO-$d_6$ + $Bu_4NOH$); $\delta$ 9.43 (d, 1H), 9.37 (s, 1H), 9.33 (d, 1H), 9.17 (s, 1H), 9.14 (s, 1H), 8.98 (s, 1H), 8.49 (d, 1H), 8.44 (d, 1H), 8.42 (d, 2H), 8.29−8.32 (m, 1H), 8.19 (d, 2H), 8.12 (d, 2H), 8.04 (d, 2H), 8.02 (s, 1H), 7.59−7.65 (m, 2H); other data were signals of $Bu_4NOH$; Anal. Calcd for $C_{38}H_{22}N_8O_4RuS_2$: C, 55.67; H, 2.70; N, 13.67; Found: C, C, 55.78; H, 2.75; N, 13.59.

**3b** (X = F): yield 76%; $^1$H NMR (300.1 MHz; DMSO-$d_6$ + $Bu_4NOH$); $\delta$ 9.42 (d, 1H), 9.23 (d, 1H), 9.21 (s, 1H), 9.04 (s, 1H), 8.92 (s, 1H), 8.32 (d, 2H), 8.22 (d, 1H), 8.00 (t, 1H), 7.92 (d, 2H), 7.85−7.89 (m, 1H), 7.63 (t, 1H), 7.46 (t, 1H), 7.40 (t, 1H), 7.23 (d, 2H), 7.10 (d, 2H); other data were signals of $Bu_4NOH$; Anal. Calcd for $C_{36}H_{22}F_2N_6O_4RuS_2$: C, 53.66; H, 2.75; N, 10.43; Found: C, 53.41; H, 2.43; N, 10.52.

**3c** (X = H): yield 83%; $^1$H NMR (300.1 MHz; DMSO-$d_6$ + $Bu_4NOH$); $\delta$ 9.42 (d, 1H), 9.31 (d, 1H), 9.28 (s, 1H), 9.15 (s, 1H), 9.12 (s, 1H), 8.99 (s, 1H), 8.37 (d, 1H), 8.29 (d, 1H), 8.23 (d, 2H), 7.93 (d, 2H), 7.84 (d, 1H), 7.69 (t, 2H), 7.60−7.63 (m, 2H), 7.54−7.57 (m, 4H), 7.51 (t, 1H); other data were signals of $Bu_4NOH$; Anal. Calcd for $C_{36}H_{24}N_6O_4RuS_2$: C, 56.17; H, 3.14; N, 10.92; Found: C, 56.41; H, 3.19; N, 10.98.

**3d** (X = OMe): yield 75%; $^1$H NMR (300.1 MHz; DMSO-$d_6$ + $Bu_4NOH$); $\delta$ 9.39 (d, 1H), 9.19 (d, 1H), 9.16 (s, 1H), 9.11 (s, 1H), 9.00 (s, 1H), 8.95 (s, 1H), 8.28 (d, 1H), 8.25 (d, 1H), 8.18 (d, 2H), 7.88 (d, 2H), 7.84 (d, 1H), 7.59 (d, 1H), 7.47 (d, 1H), 7.40 (d, 1H), 7.19 (d, 2H), 7.05 (d, 2H), 3.87 (s, 3H), 3.78 (s, 3H); other data were signals of $Bu_4NOH$; Anal. Calcd for $C_{38}H_{28}N_6O_6RuS_2$ (830.06): C, 55.00; H, 3.40; N, 10.13; Found: C, 55.11; H, 3.48; N, 10.11.

**3e** (X = $NMe_2$): yield 65%; $^1$H NMR (300.1 MHz; DMSO-$d_6$ + $Bu_4NOH$); $\delta$ 9.35 (d, 1H), 9.17 (d, 1H), 9.14 (s, 1H), 9.08 (s, 1H), 8.98 (s, 1H), 8.90 (d, 1H), 8.17 (d, 1H), 8.08 (d, 2H), 7.75 (d, 2H), 7.70 (d, 1H), 7.48 (d, 1H), 7.40 (d, 1H), 7.34 (d, 1H), 7.11 (d, 2H), 7.02 (d, 2H), 3.01 (s, 6H), 2.99 (s, 6H); other data were signals of $Bu_4NOH$; Anal. Calcd for $C_{40}H_{34}N_8O_4RuS_2$: C, 56.13; H, 4.00; N, 13.09; Found: C, 56.28; H, 4.08; N, 13.02.

**Theoretical Calculations.** DFT calculations were carried out using B3LYP* (Becke's three-parameter exchange functional (B3) and the Lee−Yang−Parr correlation functional (LYP)) and the LANL2DZ basis set.[19] All geometries were fully optimized in the ground states (closed-shell singlet $S_o$). All calculations were performed with the *Gaussian 03W* software package.[20]

**Emission Quantum Yield Calculations.** Fluorescence emission quantum yield values ($\Phi_{PL}$) of the ruthenium complexes were calculated employing the comparative method of William,[21] which involves the use of well characterized standards with known $\Phi_{PL}$ values. For this purpose, the UV−vis absorbance and corrected emission spectra of five different concentrations (1 $\mu$M ∼ 5 $\mu$M) of reference standards (Rhodamine B; Aldrich, $\Phi_{PL}$ = 1.00) and ruthenium complexes were recorded. Rhodamine B has been used in mixture of ethanol and 0.01% HCl and ruthenium complexes have been used in DMF solution. Record the UV−vis absorbance and fluorescence spectrum of sample and then integrated fluorescence intensities of the ruthenium complexes were plotted vs absorbance values. The gradients of the plots are proportional to the quantity of the quantum yield. Absolute values are calculated using the standard samples which have a fixed and known fluorescence quantum yield value, according to the following equation:

$$\Phi_X = \Phi_{ST}\left(\frac{Grad_X}{Grad_{ST}}\right)\left(\frac{\eta_X^2}{\eta_{ST}^2}\right)$$

where the subscripts ST and X denote standard and ruthenium respectively, $\Phi$ is the fluorescence quantum yield, Grad the gradient from the plot of integrated fluorescence intensity versus absorbance, and $\eta$ the refractive index of the solvent.[21]

**DSSC Fabrication.** DSSCs were fabricated as follows. Transparent conductive glass plates coated with an F-doped $SnO_2$ (FTO, purchased from Pilkington. Co. Ltd., 8 $\Omega/\gamma$) were used to prepare both the photo- and counter-electrodes. A Ti(IV) bis(ethyl acetoacetato)-diisopropoxide solution (2% *w*/*w* in 1-butanol) was spin-coated onto FTO substrates, which were then heated stepwise to 450 °C and maintained at this temperature for 20 min. Commercialized $TiO_2$ paste (Ti-Nanoxide T, Solaronix) was cast onto the heat-treated FTO substrates by the doctor-blade technique and then sintered at 450 °C for 30 min. The substrates with thick mesoporous $TiO_2$ layers (ca. 13−18 $\mu$m) were dipped into a 1:1 *tert*-butanol/acetonitrile solution of **3a**−**3e** or **N3** (0.3 mM) and kept overnight. Pt-layered counter-electrodes were prepared by spin-coating $H_2PtCl_6$ solution (0.05 M in isopropanol) onto FTO glass and then sintered at 400 °C for 30 min. The dye-adsorbed $TiO_2$ electrodes and Pt counter-electrodes were assembled into a sealed sandwich-type cell by heating at 80 °C using a hot-melt ionomer film (Surlyn) as a spacer between the electrodes. The electrolyte was composed of 0.6 M 3-hexyl-1,2-dimethyl imidazolium iodide, 0.05 M iodine, 0.05 M LiI, and 0.5 M 4-tert butylpyridine in acetonitrile. A drop of the electrolyte solution was placed in a hole drilled in the counter-electrode and driven into the cell via vacuum backfilling. Finally, the hole was sealed using additional Surlyn and a cover glass (0.1 mm thick).

**Solar Cell Efficiency.** The photoelectrochemical performance characteristics (short-circuit current $J_{sc}$ ($mA \cdot cm^{-2}$), open-circuit voltage $V_{oc}$ (V), fill factor ff, and overall energy conversion efficiency $\eta$) were measured under illumination with a 1000 W xenon lamp (Oriel, 91193) using a Keithley Model 2400. The light intensity, which was confirmed to be homogeneous over an 8 × 8 $in^2$ area, was calibrated with a Si solar cell (Fraunhofer Institute for Solar Energy Systems, Mono-Si+KG filter, Certificate No. C-ISE269) for 1 sun light intensity (AM 1.5G, 100 $mW \cdot cm^{-2}$) and was double-checked with an NREL-calibrated Si solar cell (PV Measurements, Inc.). Accidental increases in temperature inside the cell during measurement were prevented by using a cooler with a propeller. Each measurement was repeated at least three times to confirm reproducibility.

**IPCE.** Incident photon-to-current conversion efficiency (IPCE) was measured as a function of wavelength from 360 to 800 nm (PV

**Scheme 1. Synthesis Route of 3a−3e and N3 Dye**

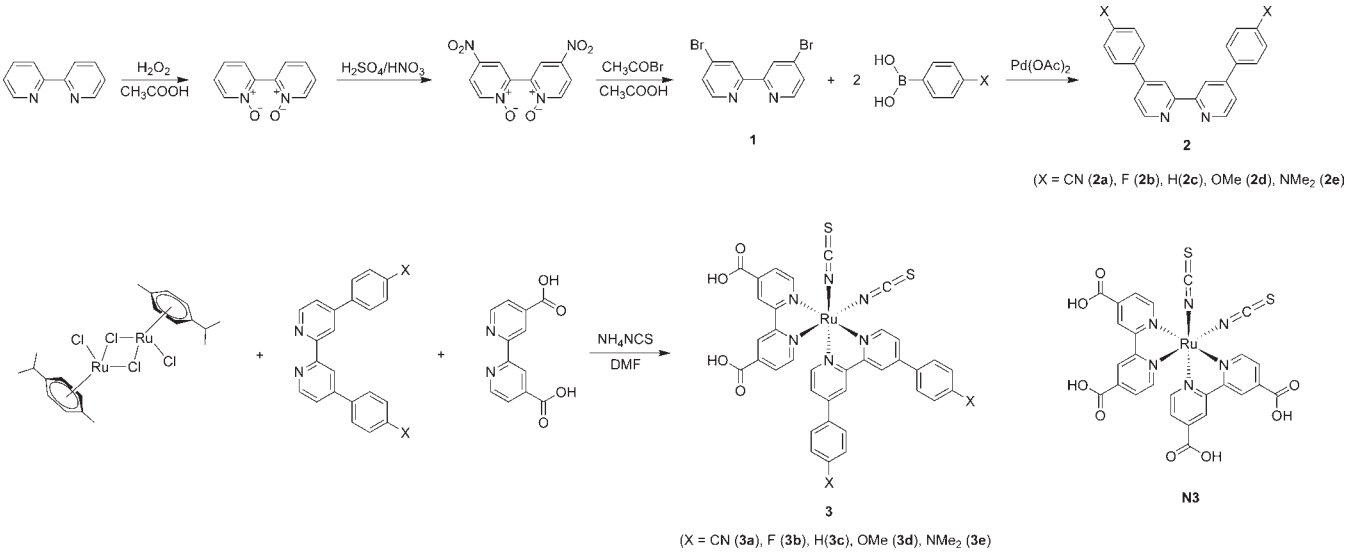


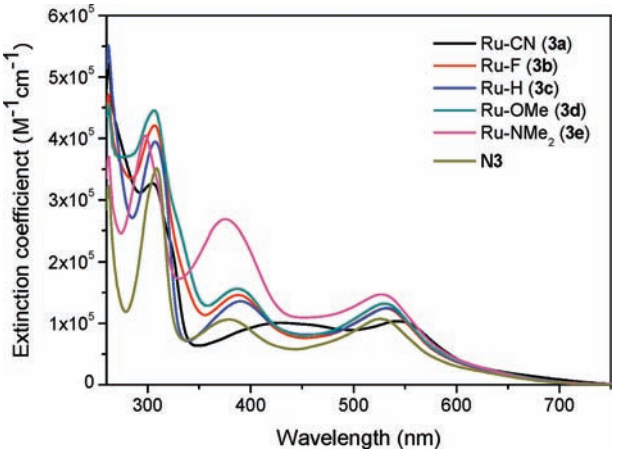


**Figure 1.** Electronic absorption spectra of **3a**−**3e** and **N3** measured in DMF.

Measurements, Inc.) using a standard tungsten-halogen lamp as monochromatic light and a broadband bias light for approximating 1 sun light intensity.

**Laser Flash Photolysis.** Nanosecond transient absorption measurements were conducted by a laser flash photolysis technique for completed DSSCs irradiated with 504 nm pulses generated by hydrogen Raman shifting of third-harmonic generation (THG, 355 nm) from a Q-switched Nd:YAG laser (Continuum, Surelite II, pulse width of 4.5 ns fwhm). A 150 W xenon arc lamp (Newport, 70525) was focused into the sample solution as the probe light for the measurements. Temporal profiles were measured with a monochromator (DongWoo Optron, Monora 500i) equipped with a photomultiplier (Zolix Instruments Co., CR 131) and a digital oscilloscope (Tektronix, TDS-784D). Reported signals are averages of 1000 events. The decay profiles for the oxidized dyes are monitored at 820 nm.

## RESULTS AND DISCUSSION

**Synthesis.** Scheme 1 outlines the synthesis of $Ru(NCS)_2LL'$. Di(*p*-X-phenyl)-2,2′-bipyridines (L′; X = CN (**2a**), F (**2b**), H (**2c**), OMe (**2d**), and $NMe_2$ (**2e**)) synthesized by Pd-catalyzed Suzuki coupling reaction were reacted with $[Ru(p\text{-cymene})Cl_2]_2$ in DMF under nitrogen to give $Ru(p\text{-X-phenyl})_2Cl_3$. The $Ru(NCS)_2LL'$ complexes were obtained by the reaction of $Ru(p\text{-X-phenyl})_2Cl_3$ with 4,4′-di(hy3droxycarbonyl)-2,2′-bipyridine (L) followed by treatment with a large excess of ammonium thiocyanate. All the products were isolated in moderate yields (65−83%) by Sephadex column followed by acid precipitation. The structures were unambiguously identified by their spectroscopic properties and elemental analyses (Experimental Section).

**Spectroscopic and Electrochemical Properties.** The UV−vis absorption spectra of **3a**−**3e** and **N3** in DMF are shown in Figure 1, and the optical data are summarized in Table 1. The absorption spectra of **3a**−**3e** consist of three bands with a spectral feature similar to that of **N3** caused by ligand-based charge transfer (LBCT) and/or MLCT transitions. It should be noted that **3a**−**3e** exhibit higher extinction coefficients than **N3** over the entire investigated region, which is attributed to the conjugation effect of the *p*-X-phenyl substituents.

The high-energy bands in the UV region between 298 and 307 nm are assigned as being dominated by the L-centered $\pi-\pi^*$ transition overlapping the L′ $\pi-\pi^*$ transition. The second absorption band (abbreviated as band I), with maxima between 375 and 428 nm, should be assigned to LBCT plus MLCT, as reported.[6a,22] The low-energy absorption band located between 527 and 542 nm, abbreviated as band II, should be the result of MLCT arising from the participation of the NCS moieties, because such a low-energy MLCT transition does not appear with related Ru(II) complexes without an NCS ligand. The absorption maxima of bands I and II depend substantially on the electron-withdrawing/donating nature of X; a systematic bathochromic shift occurs as X changes from the strong electron-donating $NMe_2$ group (**3e**) to the strong electron-withdrawing CN group (**3a**). It is of interest to note that **3a** shows a panchromatic-like absorption feature in the visible region, with the maxima of bands I and II longer by 49 and 17 nm respectively than in **N3**. Moreover, the molar extinction coefficients for bands


dx.doi.org/10.1021/ic101909e |*Inorg. Chem.* 2011, 50, 3271–3280

**Table 1. Photophysical Properties of 3a−3e and N3**

| | $\lambda_{max}$ (nm)[a]/$\varepsilon$ [ $\times 10^4$ $M^{-1}cm^{-1}$] | | | | | | | |
|---|---|---|---|---|---|---|---|---|
| Ru complex (X) | LC | band I | band II | $\lambda_{PL}$ (nm)[b] | HOMO (eV)[c] | LUMO (eV)[c] | $\Phi_{PL}$[d] ( $\times 10^{-4}$) | $\tau_{PL}$[e] (ns) |
| **3a** (CN) | 306/3.27 | 428/1.06 | 542/1.04 | 800 | −4.82 | −3.18 | 2.0 | 33.0 |
| **3b** (F) | 307/4.21 | 390/1.46 | 533/1.24 | 762 | −4.60 | −2.97 | 4.2 | 39.0 |
| **3c** (H) | 307/3.95 | 389/1.36 | 533/1.25 | 773 | −4.54 | −2.91 | 3.3 | 40.0 |
| **3d** (OMe) | 306/4.45 | 388/1.56 | 530/1.32 | 759 | −4.46 | −2.83 | 5.4 | 48.0 |
| **3e** ($NMe_2$) | 298/4.05 | 375/2.69 | 527/1.47 | 744 | −4.30 | −2.69 | 5.7 | 66.0 |
| **N3** | 309/3.51 | 379/1.06 | 525/1.07 | 764 | −4.95 | −3.24 | 4.0[f] | 60.0[g] |

[a] Measured in DMF. [b] Emission maxima observed by excitation at 530 nm. [c] HOMO and LUMO levels were determined using the following equations: $E_{HOMO}$ (eV) = $-(E_{ox} - E_{Fc|Fc+} + 4.8$ eV), $E_{LUMO}$ (eV) = $-(E_{HOMO} - E_g$; $E_g$ = absorption threshold of the Ru complexes). [d] Emission quantum yields for air-purged DMF solution. [e] Emission lifetimes for air-purged DMF solution. [f] Ref 1e. [g] Ref 9e.

**Table 2. Electrochemical Properties of 3a−3e and N3**

| | | $E_{red}$[b] | | | |
|---|---|---|---|---|---|
| | $E_{1/2}$/V[a] ($Ru^{III/II}$) V vs $Fc|Fc^+$ | $E_{pc1}$ | $E_{pc2}$ | $E_{pa1}$ | $E_{pa2}$ |
| **3a** (CN) | 0.39 | −1.84 | −2.15 | −2.04 | −1.74 |
| **3b** (F) | 0.36 | −2.01 | −2.44 | −2.30 | −1.93 |
| **3c** (H) | 0.34 | −2.00 | −2.47 | −2.20 | −1.93 |
| **3d** (OMe) | 0.31 | −2.07 | −2.49 | −2.26 | −1.99 |
| **3e** ($NMe_2$) | 0.26 | −2.19 | −2.55 | −2.33 | −2.08 |

[a] The $Ag/AgNO_3$ reference electrode was calibrated with a ferrocene/ferrocinium ($Fc|Fc^+$) redox couple. The electrochemical experiments were carried out in 0.1 M [$n$$Bu_4N$]$BF_4$/MeCN solution. [b] $E_{pc1}$ and $E_{pc2}$ denote cathodic peaks at negative scan, whereas $E_{pa1}$ and $E_{pa2}$ represent anodic peaks at reverse scan.

I and II depend substantially on the substituent X, as revealed by the decrease from the exceptionally high values of **3e** to the values of **3a** comparable with those of **N3**. All these observations clearly demonstrate that the electronic transitions of $Ru(NCS)_2LL'$ have been tuned by the choice of remote substituent X.

Table 1 also shows the emission parameters (maxima, quantum yields, and lifetimes) of **3a**−**3e** in DMF solution at 298 K, which again reveal significant dependences on the substituent X. The emission maximum moved by 56 nm, from 744 nm for **3e** to 800 nm for **3a**; the latter was longer by 36 nm than that of **N3**. The emission quantum yields showed a ∼2.8-fold difference between the highest value for **3e** and the lowest one for **3a**. The lifetimes increased systematically from 33 ns for **3a** to 66 ns for **3e**. All these results again indicate that the $^3$MLCT-state behavior of $Ru(NCS)_2LL'$ depends substantially on the remote substituent X.

Cyclic voltammetric measurements for acetonitrile solutions of **3a**−**3e** were performed under identical conditions, typically yielding pseudoreversible oxidation and reduction waves, as shown in Figure S2 (Supporting Information) for a typical trace of **3d**. The oxidation and reduction potentials obtained from the voltammograms are presented in Table 2. Whereas the oxidation potential of **3e** was significantly more positive by 0.05−0.13 V than the others, **3a**−**3d** show small variations in the oxidation waves. It is worth noting that the oxidation potential of **3a** was only slightly negative (by 0.01 V) compared with the value reported for **N3**,[9d] even though the latter has the strong electron-withdrawing carboxylic groups directly bound the bipyridine ligand. This suggests that the *p*-cyanophenyl group has an effect comparable with that of the carboxylic substituent for one-electron oxidation of the Ru(II) center.

At negative potentials versus $Fc|Fc^+$, two peaks that can be attributed to ligand-based reductions were observed.[23] As shown in Table 2, electron-withdrawing ligands clearly result in more positive shifts of redox potential. In the reduction of Ru(II) polypyridine complexes, an electron is added to the LUMO, usually the $\pi^*$ orbital of a polypyridine ligand.[24] Therefore, each of the bpy ligands L and L′ can accept an electron in each electrochemically accessible unoccupied molecular orbital. As expected, **3a**−**3e** all exhibited two clear cathodic peaks, an irreversible reduction wave $E_{pc1}$ spanning from −1.84 (**3a**) to −2.19 V (**3e**) and a reversible one $E_{pc2}$ spanning from −2.15 to −2.55 V, which might be attributable to the one-electron reduction of L and L′, respectively. The irreversibility of the first wave should arise from eq 1, that is, reductive $H_2$ evolution from the carboxylic acid groups located at the 4,4′-positions in the 2,2′-bipyridine ring.[25]

$$R - CO_2H + e^- \rightarrow R - CO_2^- + \frac{1}{2}H_2 \qquad (1)$$

**Computational Studies.** For further insights into the electronic structures of **3a**−**3e** with regard to the HOMO and LUMO levels, we performed DFT calculations using the B3LYP/6-31G* exchange correlation functional with the Los Alamos effective core potential LanL2DZ[19] as implemented in the *Gaussian03* package.[20]

Table 3 and Figure 2 summarize the results. Notably, both the HOMO and LUMO levels increase systematically as X changes from the strong electron-withdrawing CN group to the strong electron-donating $Me_2N$ group, indicating that the remote substituent X can tune the electronics of $Ru(NCS)_2LL'$. For comparison, DFT calculations were also performed for **N3** (L = L′), yielding deeper HOMO and LUMO levels than those of **3a**−**3e**. This seems reasonable because the strong electron-withdrawing $CO_2H$ groups are directly attached to the two bpy rings. The calculated HOMO/LUMO levels correlate well with the experimentally estimated values listed in Table 1. Good correlations were also found between the first reduction potentials and the LUMO levels and between the oxidation potentials and the HOMO levels. Figure 2 shows the energy levels and orbital population densities of the HOMO-1, HOMO, LUMO, and LUMO+1 for the heteroleptic Ru(II) complexes, demonstrating the exclusive population of HOMO and HOMO-1 on the Ru−$(NCS)_2$ part and the localized amplitude of LUMO on


dx.doi.org/10.1021/ic101909e |*Inorg. Chem.* 2011, 50, 3271–3280

**Table 3. Calculated Energies for 3a−3e**

| (eV) | N3 | 3a (Ru−CN) | 3b (Ru−F) | 3c (Ru−H) | 3d (Ru−OMe) | 3e (Ru−$NMe_2$) |
|---|---|---|---|---|---|---|
| LUMO+3 | −2.367 | −2.585 | −2.095 | −2.041 | −1.960 | −1.823 |
| LUMO+2 | −2.667 | −2.612 | −2.422 | −2.367 | −2.286 | −2.150 |
| LUMO+1 | −3.184 | −3.048 | −2.667 | −2.585 | −2.422 | −2.231 |
| LUMO | −3.238 | −3.184 | −2.966 | −2.912 | −2.830 | −2.694 |
| HOMO | −4.952 | −4.816 | −4.599 | −4.544 | −4.463 | −4.300 |
| HOMO-1 | −5.089 | −5.007 | −4.789 | −4.735 | −4.646 | −4.490 |
| HOMO-2 | −5.333 | −5.089 | −4.843 | −4.781 | −4.708 | −4.544 |
| HOMO-3 | −5.442 | −5.197 | −4.980 | −4.898 | −4.816 | −4.684 |
| $E_g$ | 1.714 | 1.632 | 1.633 | 1.632 | 1.633 | 1.606 |

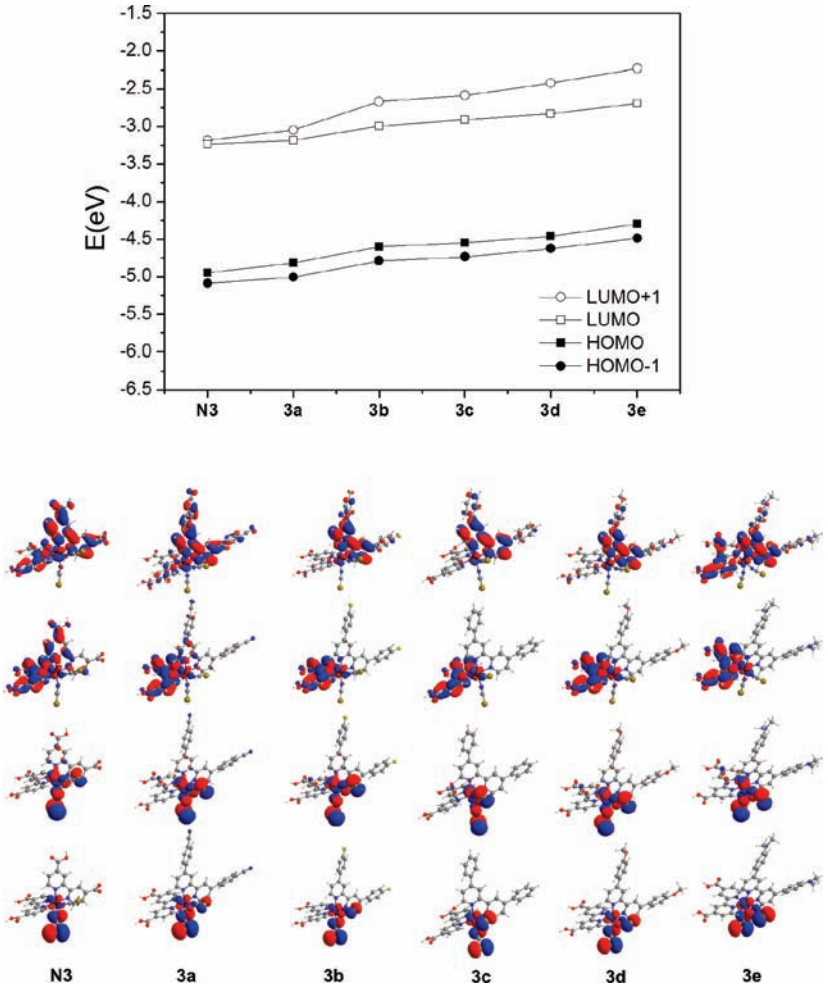


**Figure 2.** (Top) Theoretically calculated energy levels of **3a**−**3e**. HOMO−LUMO gaps are reported in eV. (Bottom) Isodensity plots for HOMO−1, HOMO, LUMO, and LUMO +1 (from bottom to top).

L, with one exception (**3a**). These features are very similar to those reported for **N3**,[26] indicating that **3a**−**3e** basically maintain the electronic structure of **N3**.

However, LUMO+1 was largely populated on L′, except for **3e**, which contains the strong electron-donating $NMe_2$ group. It is of interest to note that the energy gap between LUMO and LUMO+1 increased as X changed from the strong electron-withdrawing CN group to the strong electron-donating $NMe_2$ group, in contrast to the almost constant differences (0.18−0.19 eV) between HOMO and HOMO+1. These results should be correlated with the systematic blue-shift of band I from **3a** to **3e**, assuming the HOMO-to-LUMO+1 transition contributes considerably to band I. For **3a**, a small but non-negligible population of LUMO density exists on L′, in sharp contrast to the complete absence in the cases of **3b**−**3e**. These DFT calculations clearly showed that the HOMO/LUMO levels can be systematically tuned by changing X from the strong electron-donating $NMe_2$ group to the


dx.doi.org/10.1021/ic101909e |*Inorg. Chem.* 2011, 50, 3271–3280

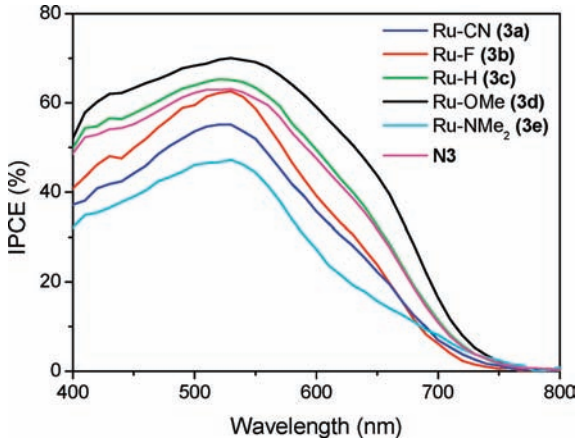


**Figure 3.** IPCE plot versus excitation wavelengths for DSSCs using **3a**−**3e** and **N3**.

strong electron-withdrawing CN group while maintaining the basic electronic structure of **N3**.

**Application of 3a−3e to Dye-Sensitized Solar Cells.** As discussed above, the present **N3**-related dyes (**3a**−**3e**) reveal uniquely tunable electronic properties associated with different X. Therefore, the application of **3a**−**3e** to DSSCs can be expected to provide clues to exploring the dye-related structure −activity relationships controlling the performance of DSSCs in solar cells. The primary requirement for DSSCs is that relevant dyes must have excited-state potentials capable of injecting an electron into the conduction band of $TiO_2$. The excited-state oxidation potentials of these dyes (<−1.55 V vs $Fc|Fc^+$) are sufficiently more negative than the conduction-band level of $TiO_2$ ($E_{CB} \approx 0.13$ V vs $Fc|Fc^+$). Another essential requirement is that the dyes must have HOMO levels that are more positive than the redox potential of the $I_3^-/I^-$ couple (−0.06 V vs $Fc|Fc^+$) for efficient reduction of the oxidized dyes to occur after electron injection. The HOMO levels of **3a**−**3e** should be positive enough for the electron transfer (ET) to proceed efficiently, as shown by the oxidation potentials (0.26−0.39 V vs $Fc|Fc^+$) listed in Table 2. In addition, the relatively high molar extinction coefficients of **3a**−**3e** over an expanded wavelength region might be beneficial for harvesting visible light. Therefore, we investigated the performance of the DSSCs in relation to the electronic properties of **3a**−**3e**.

The photovoltaic performance of DSSCs using **3a**−**3e** were studied under 1 sun (AM 1.5G, 100 mW·cm$^{-2}$) and compared with those of a standard DSSC using **N3**. Experimental conditions for cell fabrication and measurement of solar cell characteristics were carefully kept as unchanged as possible so that the cell characteristics would reflect the functions of the dyes.

Figure 3 shows the monochromatic IPCE values for devices using **3a**−**3e** and **N3**; broad curves cover almost the entire visible region from 400 to 720 nm for all of the devices. Substantial variations in IPCE were observed, depending on the devices. The efficiencies increase with increasing electron-donating power of X, reaching a maximum for the **3d**-based device, but with a large drop for **3e**, that is, **3e** < **3a** < **3b** < **N3** ≈ **3c** < **3d**. This suggests that the remote substituent X should control the DSSC's performance to a considerable degree. Alternatively, these differences might simply arise from different light-harvesting efficiencies in the dyes adsorbed on the $TiO_2$ surface. However, this is clearly not the case, as demonstrated by the absorption spectra of

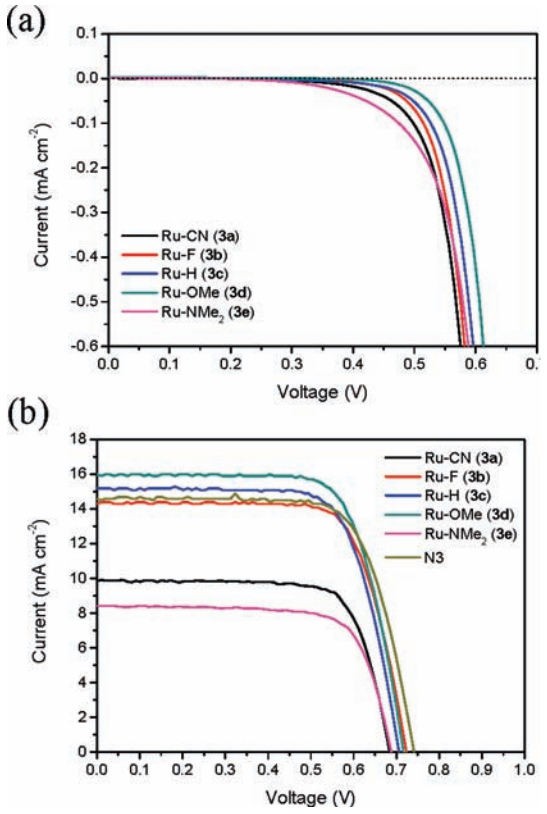


**Figure 4.** Current density−voltage curves for DSSCs using **3a**−**3e** measured (a) in the dark and (b) under 1 sun simulated sunlight illumination (AM 1.5G, 100 mW·cm$^{-2}$).

**Table 4. Photovoltaic Properties of DSSCs Using 3a−3e and N3 as a Sensitizer under 1 Sun Conditions (AM 1.5G, 100 mW·cm$^{-2}$)**

| dye (X) | $V_{oc}$ (mV) | $J_{sc}$ (mA·cm$^{-2}$) | ff (%) | $\eta$ (%) |
|---|---|---|---|---|
| **3a** (CN) | 668 | 10.0 | 73.7 | 4.90 |
| **3b** (F) | 724 | 14.3 | 73.1 | 7.59 |
| **3c** (H) | 706 | 15.2 | 71.7 | 7.72 |
| **3d** (OMe) | 717 | 16.0 | 72.4 | 8.30 |
| **3e** ($NMe_2$) | 688 | 8.41 | 73.3 | 4.24 |
| **N3** | 742 | 14.6 | 71.9 | 7.80 |

the cells taken in the absence of the electrolyte (Figure S1 of the Supporting Information).

Part a of Figure 4 shows the current−voltage characteristics of the devices in the dark, which reveal sufficient rectification effects with significantly different behavior depending on the device. The turn-on voltages associated with hole transfer from the dye-grafted $TiO_2$ electrode to the electrolyte increase in the order **3e** < **3a** < **3b** < **3c** < **3d**, similar to the IPCE behavior. Part b of Figure 4 shows the photovoltaic performances of the devices, again indicating remarkable dependences on the dyes, with a trend that parallels those of the IPCE and dark-current behavior. Table 4 summarizes the characteristic parameters abstracted from part b of Figure 4, including the open-circuit voltages ($V_{oc}$), short-circuit currents ($J_{sc}$), fill factors (ff), and power conversion efficiencies ($\eta$). The ff values are almost constant (71.7−73.7%), indicating that the device configurations are


dx.doi.org/10.1021/ic101909e |*Inorg. Chem.* 2011, 50, 3271–3280

**Chart 1. Kinetic Processes in DSSCs**

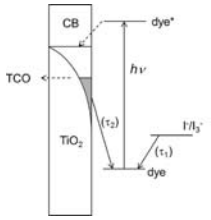


$$Dye–TiO_2 + h\nu \rightarrow Dye^{\bullet+}–TiO_2(e^-) \quad \text{electron injection}$$

$$Dye^{\bullet+}–TiO_2(e^-) + 2\,I^- \rightarrow Dye–TiO_2(e^-) + I_2^- \quad \text{ET process } (\tau_1)$$

$$Dye^{\bullet+}–TiO_2(e^-) \rightarrow Dye–TiO_2 \quad \text{CR process } (\tau_2)$$

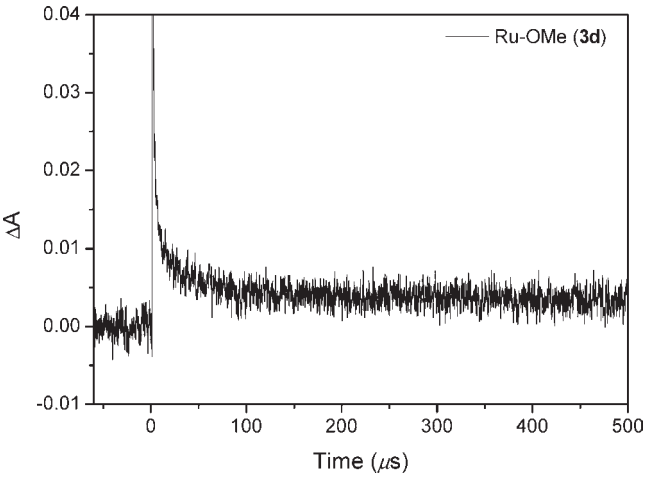


**Figure 5.** Temporal decay profile for the **3d**-based device monitored at 820 nm.

similar and the device performance reflects the electronic nature of the dyes. The $V_{oc}$ and $J_{sc}$ values are clearly poor for the device using **3a**, with the strong electron-withdrawing CN group, and still worse for the device using **3e**, with the highly electron-donating $NMe_2$ group. In contrast, the device using **3d**, with the moderately electron-donating MeO group, has the highest $J_{sc}$. Consequently, the $\eta$ values systematically increase with increasing electron-donating power of X to reach a maximum for the **3d**-based device but drop greatly for **3e**, an observation in line with the IPCE behavior. It should be noted that the **3d**-based DSSC gives the best conversion efficiency ($\eta$ = 8.30%) of the cells investigated, which is higher than that of the **N3**-based device ($\eta$ = 7.80%) measured under identical conditions.

The poor performances of the **3a**- and **3e**-based devices are reminiscent of the reported behavior of DSSCs based on Ru(NCS)$_2$LL′, with L′ = $NO_2$- or $NH_2$-substituted phenanthroline ligand.[27] For the $NO_2$-substituted ligand, the poor performance has been discussed in terms of the unusually deep LUMO level coupled with the dominant LUMO population on L′ remote from the $TiO_2$ surface, which cause inefficient electron injection from the excited-state dye into the $TiO_2$ conduction band. Although this would also work, at least in part, for the **3a** device, **3a** has a sufficiently high LUMO compared with $E_{CB}$ and a very small population of LUMO density on L′. Therefore, other factors should be considered, that is, enhanced charge recombination (CR) between the injected electrons and the oxidized dye (below). For the $NH_2$-substituted ligand, on the other hand, the device behavior has been attributed to enhanced CR between the injected electrons and the oxidized electrolyte. In the **3e** device, the charge recombination with the oxidized electrolyte should be more enhanced compared with the other devices, as indicated by the dark current behavior in part a of Figure 4. The relatively shallow HOMO level of **3e** should provide a weak driving force for ET from $I^-$ to $\mathbf{3e}^{+\bullet}$, enhancing participation in CR. Furthermore, a well-known fact that amines interact with $I_2$ to form CT complexes should be taken into consideration. Such interactions might lead to an increase in local concentration of the oxidized electrolyte in contact with the dyes, thus enhancing CR.

**Table 5. Kinetics for Electron Transport and Recombination Dynamics for 3a−3d and N3**

| | $\tau_1$ ($\mu$s) | $\tau_2$ ($\mu$s) | amplitude $A_1/A_2$ |
|---|---|---|---|
| Ru−CN (**3a**) | 0.36 | 80 | 79/21 |
| Ru−F (**3b**) | 0.40 | 177 | 80/20 |
| Ru−H (**3c**) | 0.41 | 209 | 85/15 |
| Ru−OMe (**3d**) | 0.48 | 211 | 87/13 |
| **N3** | 0.44 | 117 | 80/20 |

In general, CR between the injected electron and the oxidized dye ($Dye^{\bullet+}$) may occur in competition with ET from $I^-$ to $Dye^{\bullet+}$, with considerable effect on DSSC performance, particularly $V_{oc}$ and $J_{sc}$. The kinetic processes in DSSCs are described in Chart 1. To obtain insights into the ET and CR processes, we investigated the transient dynamics of completed DSSCs by monitoring the decay of $Dye^{\bullet+}$ absorption at 820 nm. Figure 5 shows a typical temporal decay profile for the **3d**-based device, which can be fitted to a biexponential kinetics consisting of fast ($\tau_1$) and slow ($\tau_2$) components reasonably well. Similar biexponential decays of the absorption at 820 nm were observed for the other devices as well; the decay times ($\tau_1$ and $\tau_2$) and their amplitudes ($A_1$ and $A_2$) are shown in Table 5.

It is well established that ET occurs in a time domain of 0.1−10 $\mu$s, whereas CR proceeds in a range of hundreds of microseconds or even a few milliseconds.[28] Therefore, the observed fast ($\tau_1$) and slow ($\tau_2$) kinetics can be attributed to ET and CR, respectively. As shown in Table 5, the $\tau_1$ values are fairly constant (0.36−0.48 $\mu$s), indicating that the ET process occurs at reaction rates very similar to that for the **N3** device independently of the dyes. This can be reasonably attributed to the deep HOMO levels of all the dyes compared with the redox potential of the electrolyte. In contrast, a substantial variation can be observed for the slow $\tau_2$ component, from 80 $\mu$s for the **3a**-based device to 211 $\mu$s for the **3d**-based device, indicating that the CR process is slower in the order **3a** > **N3** > **3b** > **3c** > **3d**. In line with this, the $A_1/A_2$ ratio increases systematically from 79/21 for the **3a**-based device to 87/13 for the **3d**-based device, a result associated with the decrease in the CR contribution to $Dye^{\bullet+}$ decay in the order **3a** > **N3** ≈ **3b** > **3c** > **3d**. The substantial differences in the CR kinetics between the **3a** and **3d** devices


dx.doi.org/10.1021/ic101909e |*Inorg. Chem.* 2011, 50, 3271–3280

appear to arise from the different driving forces of the CR process, as suggested by the difference of ~0.35 eV estimated from the HOMO levels of **3a** and **3d** in Tables 1 and 3. Presumably, CR would be a long-distance type of electron transfer for the electron diffusing inside $TiO_2$, so the kinetics should be sensitive to differences in the driving force. However, ET should occur at short-range because $I^-$ diffuses in solution to approach the oxidized dye closely; that is, a diffusion-controlled type of process occurs. Therefore, the slow CR in the **3d** device, associated with the dye's electronic nature, can be concluded to play an essential role in the better device performance compared with the others, whereas the poor behavior of the **3a** device should be dominated by the relatively fast CR.

## CONCLUSIONS

We have investigated the photophysical and electrochemical properties of a series of newly synthesized heteroleptic ruthenium(II) complexes, $Ru(NCS)_2LL'$ (**3a**−**3e**), and their behavior in DSSCs in an attempt to explore the structure−activity relationships associated with the dyes. We demonstrated that the remote substituent X substantially affects steady-state absorption and emission maxima and redox potentials of the dyes. These properties, which are tuned by X, have been shown to correlate well with the results of DFT calculations, which show that **3a**−**3d** maintain the electronic structure of **N3**, with exclusive orbital populations of HOMO on the $Ru(NCS)_2$ part and LUMO on L, accompanied by continuous variation in the HOMO/LUMO levels depending on X. We compared the solar-cell performance of DSSCs based on **3a**−**3e** and **N3** and found that the power-conversion efficiencies increase in the order **3e** < **3a** < **3b** < **3c** < **N3** < **3d**. Transient spectroscopic studies of the completed devices revealed that charge recombination between the photoinjected electrons and the oxidized dye is slower in the order **3a** > **N3** > **3b** > **3c** > **3d**, whereas the reaction rates for electron transfer from the electrolyte to the oxidized dye are fairly constant independent of the dyes. The close relationship between the charge-recombination kinetics and the device performance suggests that slow charge recombination is the main contributor to the efficient solar cell behavior of the **3d**-based device, whereas the poor performances of the **3a** device is likely due to fast charge recombination. A particular case is the **3e** device for which the poor solar-cell behavior has been attributed to the particular chemical nature of the $Me_2N$ substituent, which enhances another charge recombination between the injected electrons and the oxidized electrolyte as well as quenching of the excited-state dye. The present observations imply that a methodology based on fine electronic tuning of dyes provides a technique for the molecular design of optimum dyes for application to DSSCs as well as to artificial photosynthesis.

## ASSOCIATED CONTENT

**Supporting Information.** Absorption spectra of **3a**−**3e** dye-adsorbed $TiO_2$ films, and cyclic voltammogram of **3d**. This material is available free of charge via the Internet at http://pubs.acs.org.

## AUTHOR INFORMATION

### Corresponding Author

*Tel: +82-41-860-1334, fax: +82-41-867-5396, e-mail: jjpac@korea.ac.kr (C.P.); sangok@korea.ac.kr (S.O.K.).

## ACKNOWLEDGMENT

This research was supported by the Basic Science Research Program through the National Research Foundation of Korea (NRF) funded by the Ministry of Education, Science, and Technology (MEST) of Korea (2010-0018456) and by the Center for Next Generation Dye-Sensitized Solar Cells (No. 2011-0001055).

## REFERENCES

(1) (a) Nazeeruddin, M. K.; Pechy, P.; Renouard, T.; Zakeeruddin, S. M.; Humphry-Baker, R.; Comte, P.; Liska, P.; Cevey, L.; Costa, E.; Shklover, V.; Spiccia, L.; Deacon, G. B.; Bignozzi, C. A.; Grätzel, M. *J. Am. Chem. Soc.* **2001**, *123*, 1613. (b) Liu, B.; Zhu, W.; Wu, W.; Ri, K. M.; Tian, H. *J. Photochem. Photobiol., A* **2008**, *194*, 268. (c) Haque, S. A.; Handa, S.; Peter, K.; Palomares, E.; Thelakkat, M.; Durrant, J. R. *Angew. Chem., Int. Ed.* **2005**, *44*, 5740. (d) O'Regan, B.; Grätzel, M. *Nature* **1991**, *353*, 737. (e) Nazeeruddin, M. K.; Kay, A.; Rodicio, I.; Humphry-Baker, R.; Müller, E.; Liska, P.; Vlachopoulos, N.; Grätzel, M. *J. Am. Chem. Soc.* **1993**, *115*, 6382.

(2) (a) Kuciauskas, D.; Freund, M. S.; Gray, H. B.; Winkler, J. R.; Lewis, N. S. *J. Phys. Chem. B* **2001**, *105*, 392. (b) Argazzi, R.; Larramona, G.; Contado, C.; Bignozzi, C. A. *J. Photochem. Photobiol., A* **2004**, *164*, 15.

(3) (a) Ferrere, S.; Gregg, B. A. *J. Am. Chem. Soc.* **1998**, *120*, 843. (b) Monat, J. E.; McCusker, J. K. *J. Am. Chem. Soc.* **2000**, *122*, 4092. (c) Paw, W.; Connick, W. B.; Eisenberg, R. *Inorg. Chem.* **1998**, *37*, 3919.

(4) (a) Schmidt-Mende, L.; Bach, U.; Humphry-Baker, R.; Horiuchi, T.; Miura, H.; Ito, S.; Uchida, S.; Grätzel, M. *Adv. Mater.* **2005**, *17*, 813. (b) Chen, R. K.; Yang, X. C.; Tian, H. N.; Sun, L. C. *J. Photochem. Photobiol., A* **2007**, *189*, 295. (c) Howie, W. H.; Claeyssens, F.; Miura, H.; Peter, L. M. *J. Am. Chem. Soc.* **2008**, *130*, 1367. (d) Kim, C.; Choi, H.; Kim, S.; Baik, C.; Song, K.; Kang, M.-S.; Kang, S. O.; Ko, J. *J. Org. Chem.* **2008**, *73*, 7072.

(5) (a) Blart, F. E.; Lagree, M.; Villieras, M.; Boujtita, H.; El Murr, N.; Caramori, S.; Bignozzi, C. A. *J. Mater. Chem.* **2003**, *13*, 502. (b) Campbell, W. M.; Jolley, K. W.; Wagner, P.; Wagner, K.; Walsh, P. J.; Gordon, K. C.; Schmidt-Mende, L.; Nazeeruddin, M. K.; Wang, Q.; Grätzel, M.; Officer, D. L. *J. Phys. Chem. C* **2007**, *111*, 11760.

(6) (a) Campagna, S.; Puntoriero, F.; Nastasi, F.; Bergamini, G.; Balzani, V. *Top. Curr. Chem.* **2007**, *280*, 117. (b) Juris, A.; Balzani, V.; Barigelletti, F.; Campagna, S.; Belser, P.; van Zelewsky, A. *Coord. Chem. Rev.* **1988**, *84*, 85. (c) Kalyanasundaram, K. *Coord. Chem. Rev.* **1982**, *46*, 159.

(7) (a) Youngblood, W. J.; Lee, S.-H. A.; Kobayashi, Y.; Hernandez-Pagan, E. A.; Hoertz, P. G.; Moore, T. A.; Moore, A. L.; Gust, D.; Mallouk, T. E. *J. Am. Chem. Soc.* **2009**, *131*, 926. (b) Youngblood, W. J.; Lee, S.-H. A.; Kobayashi, Y.; Mallouk, T. E. *Acc. Chem. Res.* **2009**, *42*, 1966.

(8) (a) Ishida, H.; Tanaka, K.; Tanaka, T. *Organometallics* **1987**, *6*, 181. (b) Takeda, H; Ishitani, O. *Coord. Chem. Rev.* **2010**, *254*, 346and references therein..

(9) (a) Grätzel, M. *Nature* **2001**, *414*, 338. (b) Hagfeldt, A.; Grätzel, M. *Acc. Chem. Res.* **2000**, *33*, 269. (c) Morandeira, A.; Lopez-Duarte, I.; Martinez-Diaz, M. V.; O'Regan, B.; Shuttle, C.; Haji-Zainulabidin, N. A.; Torres, T.; Palomares, E.; Durrant, J. *J. Am. Chem. Soc.* **2007**, *129*, 9250. (d) Chen, C. Y.; Wu, S. J.; Wu, C. G.; Chen, J. G.; Ho, K. C. *Angew. Chem., Int. Ed.* **2006**, *45*, 5822. (e) Argazzi, R.; Bignozzi, C. A.; Hasselmann, G. M.; Meyer, G. J. *Inorg. Chem.* **1998**, *37*, 4533. (e) Grätzel, M. *J. Photochem. Photobiol., C* **2003**, *4*, 145. (f) Garcia, C. G.; Iha, N. Y. M. *Int. J. Photoenergy* **2001**, *3*, 131.

(10) (a) Chen, C.-Y.; Lu, H.-C.; Wu, C.-G.; Chen, J.-G.; Ho, K.-C. *Adv. Funct. Mater.* **2007**, *17*, 29. (b) Lee, C.; Yum, J.-H.; Choi, H.; Kang, S. O.; Ko, J.; Humphry-Baker, R.; Grätzel, M.; Nazeeruddin, M. K. *Inorg. Chem.* **2008**, *47*, 2267.

(11) Anderson, P. A.; Strouse, G. F.; Treadway, T. A.; Keene, F. R.; Meyer, T. J. *Inorg. Chem.* **1994**, *33*, 3863.

(12) (a) Jiang, K.-J.; Masaki, N.; Xia, J.; Noda, S.; Yanagida, S. *Chem. Commun.* **2006**, 2460. (b) Chen, C.-Y.; Wu, S.-J.; Li, J.-Y.; Wu, C.-G.;

Chen, J.-G.; Ho, K.-C. *Adv. Mater.* **2007**, *19*, 3888. (c) Abbotto, A.; Barolo, C.; Bellotto, L.; De Angelis, F.; Grätzel, M.; Manfredi, N.; Marinzi, C.; Fantacci, S.; Yum, J.-H.; Nazeeruddin, M. K. *Chem. Commun.* **2008**, 5318. (d) Shi, D.; Pootrakulchote, N.; Li, R.; Gui, J.; Wang, Y.; Zakeeruddin, S. M.; Grätzel, M.; Wang, P. *J. Phys. Chem. C* **2008**, *112*, 17046.

(13) Gao, F.; Wang, Y.; Zhang, J.; Shi, D.; Wang, M.; Humphry-Baker, R.; Wang, P.; Zakeeruddin, S. M.; Grätzel, M. *Chem. Commun.* **2008**, 2635.

(14) (a) Wang, P.; Zakeeruddin, S. M.; Moser, J.-E.; Humphry-Baker, R.; Comte, P.; Aranyos, V.; Hagfeldt, A.; Nazeeruddin, M. K.; Grätzel, M. *Adv. Mater.* **2004**, *16*, 1806. (b) Wang, P.; Klein, C.; Humphry-Baker, R.; Zakeeruddin, S. M.; Grätzel, M. *J. Am. Chem. Soc.* **2005**, *127*, 808. (c) Kuang, D.; Klein, C.; Ito, S.; Moser, J.-E.; Humphry-Baker, R.; Evans, N.; Duriaux, F.; Grätzel, C.; Zakeeruddin, S. M.; Grätzel, M. *Adv. Mater.* **2007**, *19*, 1133.

(15) Wang, P.; Klein, C.; Humphry-Baker, R.; Zakeeruddin, S. M.; Gräztel, M. *J. Am. Chem. Soc.* **2005**, *127*, 808.

(16) (a) Islam, A.; Ikeda, N.; Yoshimura, A.; Ohno, T. *Inorg. Chem.* **1998**, *37*, 3093. (b) Heimer, T. A.; Heilweil, E. J.; Bignozzi, C. A.; Meyer, G. J. *J. Phys. Chem. A* **2000**, *104*, 4256. (c) Ruite, S.; Kohle, O.; Pechy, P. *Inorg. Chim. Acta* **1997**, *261*, 129. (d) Islam, A.; Sugihara, H.; Singh, L. P.; Hara, K. *Inorg. Chim. Acta* **2001**, *322*, 7.

(17) Islam, A.; Sugihara, H.; Hara, K.; Singh, L. P.; Katoh, R.; Yanagida, M.; Takahashi, Y.; Murata, S.; Arakawa, H.; Fujihashi, G. *Inorg. Chem.* **2001**, *40*, 5371.

(18) Brink, G. -J.; Arends, I. W. C. E.; Hoogenraad, M.; Verspui, G.; Sheldon, R. A. *Adv. Synth. Catal.* **2003**, *345*, 497.

(19) Wadt, W. R.; Hay, P. J. *J. Chem. Phys.* **1985**, *82*, 270.

(20) Frisch, M. J.; Trucks, G. W.; Schlegel, H. B.; Scuseria, G. E.; Robb, M. A.; Cheeseman, J. R.; Montgomery, J. A., Jr.; Vreven, T.; Kudin, K. N.; Burant, J. C.; Millam, J. M.; Iyengar, S. S.; Tomasi, J.; Barone, V.; Mennucci, B.; Cossi, M.; Scalmani, G.; Rega, N.; Petersson, G. A.; Nakatsuji, H.; Hada, M.; Ehara, M.; Toyota, K.; Fukuda, R.; Hasegawa, J.; Ishida, M.; Nakajima, T.; Honda, Y.; Kitao, O.; Nakai, H.; Klene, M.; Li, X.; Knox, J. E.; Hratchian, H. P.; Cross, J. B.; Adamo, C.; Jaramillo, J.; Gomperts, R.; Stratmann, R. E.; Yazyev, O.; Austin, A. J.; Cammi, R.; Pomelli, C.; Ochterski, J. W.; Ayala, P. Y.; Morokuma, K.; Voth, G. A.; Salvador, P.; Dannenberg, J. J.; Zakrzewski, V. G.; Dapprich, S.; Daniels, A. D.; Strain, M. C.; Farkas, O.; Malick, D. K.; Rabuck, A. D.; Raghavachari, K.; Foresman, J. B.; Ortiz, J. V.; Cui, Q.; Baboul, A. G.; Clifford, S.; Cioslowski, J.; Stefanov, B. B.; Liu, G.; Liashenko, A.; Piskorz, P.; Komaromi, I.; Martin, R. L.; Fox, D. J.; Keith, T., Al-Laham, M. A.; Peng, C. Y.; Nanayakkara, A.; Challacombe, M.; Gill, P. M. W.; Johnson, B.; Chen, W.; Wong, M. W.; Gonzalez, C.; Pople, J. A. *Gaussian 03W*, Rev. 6.0; Gaussian, Inc.: Pittsburgh PA, 2003.

(21) Williams, A. T. R.; Winfield, S. A.; Miller, J. N. *Analyst* **1983**, *108*, 1067.

(22) (a) Jiang, K.-J.; Masaki, N.; Xia, J.-B.; Noda, S.; Yanagida, S. *Chem. Commun.* **2006**, 2460. (b) Chen, C.-Y.; Wu, S.-J.; Wu, C.-G.; Chen, J.-G.; Ho, K.-C. *Angew. Chem., Int. Ed.* **2006**, *45*, 5822. (c) Karthikeyan, C. S.; Wietasch, H.; Thelakkat, M. *Adv. Mater.* **2007**, *19*, 1091. (d) Chen, C.-Y.; Wu, S.-J.; Li, J.-Y.; Wu, C.-G.; Chen, J.-G.; Ho, K.-C. *Adv. Mater.* **2007**, *19*, 3888. (e) Gao, F.; Wang, Y.; Zhang, J.; Shi, D.; Wang, M.; Humphry-Baker, R.; Wang, P.; Zakeeruddin, S. M.; Gräztel, M. *Chem. Commun.* **2008**, 2577. (f) Lee, C.; Yum, J.-H.; Choi, H.; Kang, S. O.; Ko, J.; Humphry-Baker, R.; Gräztel, M.; Nazeeruddin, M. K. *Inorg. Chem.* **2008**, *47*, 2267. (g) Chen, C.-Y.; Chen, J.-G.; Wu, S.-J.; Li, J.-Y.; Wu, C.-G.; Ho, K.-C. *Angew. Chem., Int. Ed.* **2008**, *47*, 7342. (h) Mater, F.; Ghaddar, T. H.; Walley, K.; DosSanto, T.; Durrant, J. R.; O'Regan, B. *J. Mater. Chem.* **2008**, *18*, 4246.

(23) (a) Webster, R. D.; Bond, A. M.; Schmidt, T. *J. Chem. Soc., Perkin Trans. 2* **1995**, *2*, 1365. (b) Balzani, V.; Juris, A.; Venturi, M.; Campagna, S.; Serroni, S. *Chem. Rev.* **1996**, *96*, 759.

(24) (a) Bhattacharya, S. *Polyhedron* **1993**, *12*, 235. (b) Tokel-Takvoryan, N. E.; Hemingway, R. E.; Bard, A. J. *J. Am. Chem. Soc.* **1973**, *95*, 6582. (c) Morris, D. E.; Hanck, K. W.; DeArmond, M. K. *Inorg. Chem.* **1985**, *24*, 977.

(25) Sawyer, D. T.; Sobkowiak, A.; Roberts, J. L. Jr. *Electrochemistry for Chemists*, John Wiley & Sons, Inc.: New York, 1995; ch. 8 and 12.

(26) Fantacci, S.; De Angelis, F.; Selloni, A. *J. Am. Chem. Soc.* **2003**, *125*, 4381.

(27) Reynal, A.; Forneli, A.; Martinez-Ferrero, E.; Sánchez-Díaz, A.; Vidal-Ferran, A.; O'Regan, B. C.; Palomares, E. *J. Am. Chem. Soc.* **2008**, *130*, 13558.

(28) (a) Tachibana, Y.; Moser, J. E.; Gräztel, M.; Klug, D. R.; Durrant, J. R. *J. Phys. Chem. B* **2002**, *106*, 20056. (b) Haque, S. A.; Palomares, E.; Cho, B. M.; Green, A. N. M.; Hirata, N.; Klug, D. R.; Durrant, J. R. *J. Am. Chem. Soc.* **2005**, *127*, 3456.